BIOLOGICAL
CRYSTALLOGRAPHY

ISSN: 1399-0047
journals.iucr.org/d

Superoxide reductase from *Giardia intestinalis*: structural characterization of the first SOR from a eukaryotic organism shows an iron centre that is highly sensitive to photoreduction

Cristiana M. Sousa, Philippe Carpentier, Pedro M. Matias, Fabrizio Testa, Filipa Pinho, Paolo Sarti, Alessandro Giuffrè, Tiago M. Bandeiras and Célia V. Romão

Acta Cryst. (2015). D**71**, 2236–2247

BIOLOGICAL CRYSTALLOGRAPHY

ISSN 1399-0047

Superoxide reductase from *Giardia intestinalis*: structural characterization of the first SOR from a eukaryotic organism shows an iron centre that is highly sensitive to photoreduction

Cristiana M. Sousa,[a,b] Philippe Carpentier,[c] Pedro M. Matias,[a,b] Fabrizio Testa,[d] Filipa Pinho,[b] Paolo Sarti,[d] Alessandro Giuffrè,[e]* Tiago M. Bandeiras[a,b] and Célia V. Romão[a]*

[a]Instituto de Tecnologia Química e Biológica, António Xavier Universidade Nova de Lisboa, Avenida da República, 2780-157 Oeiras, Portugal, [b]Instituto de Biologia Experimental e Tecnológica, Apartado 12, 2781-901 Oeiras, Portugal, [c]Structural Biology Group, ESRF – The European Synchrotron, CS40220, 38043 Grenoble CEDEX 9, France, [d]Department of Biochemical Sciences, Istituto Pasteur–Fondazione Cenci Bolognetti, Sapienza University of Rome, 00185 Rome, Italy, and [e]CNR Institute of Molecular Biology and Pathology, 00185 Rome, Italy. *Correspondence e-mail: alessandro.giuffre@uniroma1.it, cmromao@itqb.unl.pt

Received 5 March 2015
Accepted 24 August 2015

Edited by E. F. Garman, University of Oxford, England

Keywords: oxidative stress; superoxide reductase; radiation damage; eukaryotes; visible spectroscopy.

PDB reference: superoxide reductase, 4d7p

Supporting information: this article has supporting information at journals.iucr.org/d

Superoxide reductase (SOR), which is commonly found in prokaryotic organisms, affords protection from oxidative stress by reducing the superoxide anion to hydrogen peroxide. The reaction is catalyzed at the iron centre, which is highly conserved among the prokaryotic SORs structurally characterized to date. Reported here is the first structure of an SOR from a eukaryotic organism, the protozoan parasite *Giardia intestinalis* (*Gi*SOR), which was solved at 2.0 Å resolution. By collecting several diffraction data sets at 100 K from the same flash-cooled protein crystal using synchrotron X-ray radiation, photoreduction of the iron centre was observed. Reduction was monitored using an online UV–visible microspectrophotometer, following the decay of the 647 nm absorption band characteristic of the iron site in the glutamate-bound, oxidized state. Similarly to other 1Fe-SORs structurally characterized to date, the enzyme displays a tetrameric quaternary-structure arrangement. As a distinctive feature, the N-terminal loop of the protein, containing the characteristic EKHxP motif, revealed an unusually high flexibility regardless of the iron redox state. At variance with previous evidence collected by X-ray crystallography and Fourier transform infrared spectroscopy of prokaryotic SORs, iron reduction did not lead to dissociation of glutamate from the catalytic metal or other structural changes; however, the glutamate ligand underwent X-ray-induced chemical changes, revealing high sensitivity of the *Gi*SOR active site to X-ray radiation damage.

1. Introduction

Reactive oxygen species (ROS), formed by the partial reduction of dioxygen, can be involved in both redox biology and oxidative stress (Halliwell & Gutteridge, 1984; Schieber & Chandel, 2014). Serving as signalling molecules, ROS have been attributed a key role in the regulation of numerous physiological processes, such as cellular differentiation and tissue regeneration (Schieber & Chandel, 2014). On the other hand, the same species can also oxidatively damage, and thus impair, many molecules essential for life, such as lipids, DNA and proteins (Imlay, 2003; Halliwell, 2007). Therefore, it is crucial for living organisms to harbour ROS-detoxifying systems to control the physiological levels of these reactive species (Halliwell, 2007). The superoxide anion ($O_2^{\bullet -}$) is a well known ROS formed *via* one-electron reduction of dioxygen

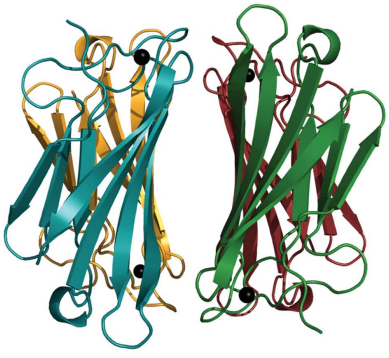

that adopts an electronic structure with an unpaired electron conferring characteristic radical reactivity (Halliwell & Gutteridge, 1984; Bertini, 1994; Sheng *et al.*, 2014; Fridovich, 1997). Two $O_2^{\bullet -}$-detoxifying enzymes have been described to date: superoxide dismutase (SOD), which catalyzes the dismutation of $O_2^{\bullet -}$ to H_2O and O_2, and superoxide reductase (SOR), which reduces $O_2^{\bullet -}$ to hydrogen peroxide (Sheng *et al.*, 2014).

Initially identified only in anaerobic and microaerobic prokayotes (Abreu *et al.*, 2001; Chen *et al.*, 1994; Jenney *et al.*, 1999; Lombard, Fontecave *et al.*, 2000; Lombard, Touati *et al.*, 2000; Moura *et al.*, 1990), SORs are currently known to also be encoded in aerobic organisms such as *Phaeodactylum tricornutum* and *Monosiga brevicollis* (Lucchetti-Miganeh *et al.*, 2011), as well as in eukaryotes such as the protozoan parasite *Giardia intestinalis* (Testa *et al.*, 2011). SORs can generally be classified according to the number of metal centres as either 2Fe-SORs (formerly named desulfoferrodoxins; Dfxs) with two iron centres or 1Fe-SORs (originally called neelaredoxins; Nlrs) with a single iron centre. The catalytic iron centre, also known as centre II, is solvent-exposed and is conserved in all SORs structurally characterized to date (Pinto *et al.*, 2010; Sheng *et al.*, 2014; Nivière & Fontecave, 2004).

Based on X-ray crystallographic and Fourier transform infrared (FTIR) spectroscopic studies of prokaryotic SORs (Berthomieu *et al.*, 2002; Yeh *et al.*, 2000; Horch *et al.*, 2014), and depending on the redox state, the catalytic iron centre has been proposed to adopt two different coordination geometries: (i) square pyramidal, in the pentacoordinate ferrous state, with four N atoms from histidine imidazoles in the equatorial plane and a cysteine sulfur in the axial position, or (ii) octahedral, in the hexacoordinate ferric state, with the vacant axial coordination position occupied by a carboxylate O atom from a glutamate located in the characteristic **EK**HxP motif (the residues in bold are conserved among SORs and have been proposed to be involved in the catalytic mechanism of superoxide anion reduction). Upon iron reduction, the site is expected to switch from the octahedral coordinated geometry with an iron-bound glutamate (‘closed conformation’) to the ‘open conformation’, with the displaced glutamate allowing substrate binding. Concomitantly, the glutamate-flanking lysine in the **EK**HxP motif moves from a solvent-exposed position to a new site pointing towards the iron centre. The ‘closed conformation’ has been observed in the crystallographic structures of the 1Fe-SORs from *Pyrococcus furiosus* (Yeh *et al.*, 2000) and *Pyrococcus horikoshii* (PDB entry 2hvb; Riken Structural Genomics/Proteomics Initiative, unpublished work). In the other SOR structures the ‘open conformation’ has been reported, in which a lysine residue occupies a structural position suitable to stabilize a peroxo intermediate, as proposed for the *Desulfoarculus baarsii* 2Fe-SOR (Adam *et al.*, 2004; Katona *et al.*, 2007).

The iron active centre of SOR has been shown to be sensitive to photoreduction by X-ray radiation (Adam *et al.*, 2004; Katona *et al.*, 2007; Yeh *et al.*, 2000; Clay *et al.*, 2002). Partial photoreduction of the *P. furiosus* 1Fe-SOR has been proposed to account for the two iron-coordination geometries that were observed in different subunits of the protein tetramer (Yeh *et al.*, 2000). By monitoring metal reduction by online microspectrophotometry in crystals of a glutamate-lacking (E47A) mutant of *D. baarsii* 2Fe-SOR co-crystallized with ferricyanide, Adam and coworkers (Adam *et al.*, 2004) found that a radiation dose of only 1.6 MGy, which is 5.3% of the experimental dose limit (Owen *et al.*, 2006), was able to promote protein reduction without any indication of a degradation effect on the diffraction patterns. In spite of the observed photoreduction, the *D. baarsii* 2Fe-SOR crystal structures always retained the ‘open conformation’, with the lysine of the **EK**HxP motif occupying a position suitable to stabilize catalytic intermediates, either hydro-peroxo or water (Adam *et al.*, 2004; Katona *et al.*, 2007). This could be owing to the fact that the solved structures resulted either from the E47A mutant (Adam *et al.*, 2004) or from the oxidized state in the protonated form (Katona *et al.*, 2007). Although no redox-linked structural changes were observed during photoreduction in the experiments of Adam, Katona and coworkers (Adam *et al.*, 2004; Katona *et al.*, 2007), this experimental approach proved to be useful in that it allowed the identification of small structural changes at atomic resolution in the iron-centre coordination sphere after X-ray exposure. By using the same approach, in the present work the first X-ray crystallographic three-dimensional structure of an SOR was obtained from a eukaryotic organism, the 1Fe-SOR from the protozoan parasite *G. intestinalis* (*Gi*SOR; 12.5 kDa per monomer, 111 amino-acid residues), and the effect of iron photoreduction on the protein structure was studied.

2. Materials and methods

2.1. Protein production

The expression and purification of *G. intestinalis* SOR were performed as described previously (Testa *et al.*, 2011). After purification, the protein was stored at −80°C at a concentration of 1 mg ml^{-1} in 50 m*M* Tris–HCl pH 7.5. Based on thermal shift screening assays carried out according to previous protocols (Santos *et al.*, 2012; Ericsson *et al.*, 2006; Niesen *et al.*, 2007), the thermal stability of the protein was found to be significantly higher in 100 m*M* 3-(*N*-morpholino)-propanesulfonic acid (MOPS) pH 7.0. Therefore, prior to crystallization, the protein buffer was exchanged to 100 m*M* MOPS pH 7.0 plus 10 m*M* NaCl by size-exclusion chromatography (Superdex 200 XK 16/60; GE Healthcare) at 4°C. Afterwards, the eluted protein was immediately concentrated to 12 mg ml^{-1} for crystallization screening.

2.2. Protein crystallization and cryoprotection

Crystallization screening was performed using the hanging-drop vapour-diffusion technique in a 48-well plate from Hampton Research using Molecular Dimensions Structure Screens 1 and 2. 1 µl drops consisting of protein solution and reservoir solution mixed in a 1:1 ratio were equilibrated against 100 µl reservoir solution. From the best hit, which contained solely 35%(*v*/*v*) dioxane, optimization was

Table 1
Data-collection, processing and phase-refinement statistics for the *Gi*SOR in-house SAD data set.

Values in parentheses are for the highest resolution shell.

Data-collection and processing statistics	
Wavelength (Å)	1.5418
Space group	*I*23
Unit-cell parameter (Å)	a = 90.71
Resolution range (Å)	28.7–1.95 (2.05–1.95)
Scan type	ω
Total angular range† (°)	296.25
Total No. of frames†	1185
Exposure time per frame (s)	60
No. of observations	172517 (15109)
Unique reflections	9222 (1257)
$\langle I/\sigma(I)\rangle$	25.4 (3.3)
R_{merge}‡ (%)	6.7 (50.8)
$R_{\text{p.i.m.}}$§ (%)	1.5 (16.2)
Completeness (%)	99.9 (100.0)
Multiplicity	18.7 (12.0)
Wilson B (Å^2)	27.2
No. of molecules in asymmetric unit	1
V_{M}¶ (Å^3 Da^{-1})	2.49
Estimated solvent content¶ (%)	50.6
Phase-refinement statistics	
Phasing power, anomalous	0.752
Anomalous R_{cullis}	0.889
SHARP FOM, acentric	0.227
SHARP FOM, centric	0.060
SHARP FOM, overall	0.201
Density-modification statistics	
Overall $\vert E^2\vert$ correlation††	0.721
FOM after final *DM* run††	0.830

† In five different crystal settings. ‡ The merging R factor $R_{\text{merge}} = \sum_{hkl}\sum_i |I_i(hkl) - \langle I(hkl)\rangle| / \sum_{hkl}\sum_i I_i(hkl) \times 100$, where $I_i(hkl)$ is the intensity measured for a unique Bragg reflection with indices hkl and $\langle I(hkl)\rangle$ is the average intensity for multiple measurements of this reflection. § The precision-independent R factor $R_{\text{p.i.m.}} = \sum_{hkl}\{1/[N(hkl) - 1]\}^{1/2} \sum_i |I_i(hkl) - \langle I(hkl)\rangle| / \sum_{hkl}\sum_i I_i(hkl) \times 100$, where $I_i(hkl)$ is the observed intensity, $\langle I(hkl)\rangle$ is the average intensity of multiple observations of symmetry-related reflections and $N(hkl)$ is the multiplicity (Weiss, 2001). ¶ According to Matthews (1968). †† From *SHARP*, optimizing the density-modification procedure (*SOLOMON* followed by a final *DM* run; Abrahams & Leslie, 1996).

performed in 24-well plates (Hampton Research), varying both the concentration of precipitant and the protein:reservoir ratio in 2–3 µl drops equilibrated against 500 µl reservoir. No buffer pH optimization was performed; the pH (7.0) was the same as in the protein solution. Blue cubic crystals with maximum dimensions of 150 × 150 × 150 µm were obtained after 1 d in 24%(*v*/*v*) dioxane at protein:precipitant ratios of 2:0.1, 2.5:0.1 and 3:0.1 µl. Owing to the volatility of dioxane, crystal handling was not straightforward, as the crystals quickly dissolved a few seconds after opening the drop cover slip. To overcome this problem, 35%(*w*/*v*) glycerol was immediately added to the drop to a final volume of 6–10 µl; this prevented the rapid evaporation of dioxane, thus allowing normal crystal handling and cryoprotection.

2.3. Data collection and processing

An initial data set was collected in-house to 1.95 Å resolution with high multiplicity at 100 K. For structure determination, the single-wavelength anomalous dispersion (SAD) method was employed using the anomalous signal of the Fe atom in the active site of the enzyme. Diffraction images collected using Cu *Kα* radiation and a Bruker AXS PLATINUM^{135} CCD detector system coupled to a Bruker AXS MICROSTAR I rotating-anode X-ray generator with Montel mirrors were processed with *SAINT* and scaled using *SADABS* as part of the Bruker AXS *Proteum* software suite (Table 1).

To obtain better data sets, the *Gi*SOR crystals were tested on beamline ID14-4 at the European Synchrotron Radiation Facility (ESRF), Grenoble, France (McCarthy *et al.*, 2009). The data were acquired at a wavelength of 0.98008 Å using φ scans and an ADSC Q315r CCD detector. The data-collection strategy consisted of 35 images with a $\Delta\varphi$ of 1.15° per image, corresponding to a total angular range of 40.25°. Seven different data sets were collected from the same flash-cooled crystal at 100 K by consecutively rotating the crystal through 40.25° per data set (total rotation of 281.75°). The first data set (ds1) was collected to 2.0 Å resolution and was the only one that was deposited in the PDB. The ID14-4 beamline was equipped with an online UV–visible microspectrophotometer coupled to the diffractometer (McGeehan *et al.*, 2009), which allowed measurement of the visible spectrum before and after the collection of each data set in order to monitor the changes in the oxidation state of the protein during data collection. The images obtained for each diffraction data set were integrated and scaled with *XDS* (Kabsch, 2010), merged with *SCALA* and converted to structure factors with *CTRUNCATE* in the *CCP*4 suite (Winn *et al.*, 2011; Collaborative Computational Project, Number 4, 1994). For data sets 2–7 (ds2–ds7), the crystal-to-detector distance was fixed using the refined value obtained from data set 1 (ds1). Data-collection and processing statistics are presented in Table 2.

2.4. Structure determination and refinement

The structure of *Gi*SOR was determined by the SAD method using the 1.95 Å resolution data set collected in-house. For clarity, this structure will be denoted *Gi*SOR$_{\text{ih}}$. Using the *HKL2MAP* (Pape & Schneider, 2004) graphical user interface, the SAD data set was scaled and analyzed with *SHELXC* (Sheldrick, 2008), while the single Fe^{3+}-ion position was determined with *SHELXD* (Schneider & Sheldrick, 2002; Sheldrick, 2008) and the phase problem was solved with *SHELXE* (Sheldrick, 2002). All 100 trials in *SHELXD* gave the same solution, with correlation coefficients of ∼38.0%, and the *SHELXE* calculations allowed clear discrimination between the correct and inverted substructures. The phases derived from the SAD data were improved using maximum-likelihood heavy-atom parameter refinement in *autoSHARP* (Vonrhein *et al.*, 2007). A subsequent optimizing density-modification procedure using *SOLOMON* (Abrahams & Leslie, 1996) suggested a solvent content of 52.5% and the presence of one monomer in the asymmetric unit. Centroid *SHARP* phases were further improved by density modification with *DM* (Cowtan, 1994). Using the 1.95 Å resolution density-modified phases from *SOLOMON*, 74 of the 111 expected protein residues in the asymmetric unit were built and automatically docked into sequence with *ARP*/*wARP* v.6.1.1 (Perrakis *et al.*, 1999), with R and R_{free} values of 0.271 and

Table 2

Data-collection and processing statistics for the *Gi*SOR synchrotron data sets.

Values in parentheses are for the highest resolution shell.

Data set	ds1	ds2	ds3	ds4	ds5	ds6	ds7
Dose† (MGy)	0.05	0.10	0.15	0.26	0.36	0.52	0.60
Unit-cell parameter (Å)	a = 90.27	a = 90.31	a = 90.44	a = 90.40	a = 90.55	a = 90.55	a = 90.47
Resolution range (Å)	31.92–2.00 (2.11–2.00)	36.86–2.45 (2.59–2.45)	45.22–2.65 (2.81–2.65)	36.90–2.25 (2.25–2.38)	36.96–2.05 (2.17–2.05)	32.01–1.95 (2.07–1.95)	36.93–1.90 (2.01–1.90)
Exposure time per frame (s)	0.10	0.10	0.10	0.20	0.20	0.20	0.20
No. of observations	41069 (6011)	22320 (3495)	17793 (2813)	22296 (3491)	37712 (5853)	44152 (7111)	46845 (6898)
Unique reflections	8422 (1217)	4659 (737)	3713 (584)	5862 (922)	7880 (1258)	9137 (1462)	9846 (1544)
$\langle I/\sigma(I)\rangle$	13.1 (2.2)	12.7 (2.37)	12.2 (2.3)	12.6 (2.3)	13.8 (2.5)	16.7 (2.9)	16.5 (2.5)
$R_{\rm merge}$‡ (%)	8.2 (77.6)	11.3 (69.3)	13.8 (80.2)	8.4 (60.8)	7.5 (66.8)	5.9 (59.3)	5.2 (56.1)
$R_{\rm meas}$§ (%)	9.2 (87.0)	12.7 (77.9)	15.5 (90.1)	9.6 (70.1)	8.5 (67.3)	6.6 (66.4)	5.9 (63.6)
$R_{\rm p.i.m.}$¶ (%)	4.1 (39.0)	5.7 (36.7)	6.9 (40.0)	4.5 (34.5)	3.8 (31.0)	2.9 (30.6)	2.6 (30.7)
Completeness (%)	99.9 (100)	99.4 (98.4)	99.6 (98.5)	94.2 (95.7)	98.6 (97.7)	99.6 (99.9)	99.0 (97.0)
Multiplicity	4.9 (4.9)	4.8 (4.7)	4.8 (4.8)	3.9 (3.8)	4.8 (4.7)	4.8 (4.9)	4.8 (4.5)
Mosaicity (°)	0.22	0.25	0.22	0.28	0.27	0.27	0.31
Wilson B factor (Å^2)	31.8	45.4	41.0	40.8	40.2	38.0	38.4
$V_{\rm M}$†† (Å^3 Da^{-1})	2.45	2.46	2.47	2.46	2.48	2.48	2.47
Estimated solvent content (%)	49.92	49.98	50.20	50.12	50.38	50.37	50.25
$R_{\rm scaling}$‡‡	—	0.075	0.096	0.091	0.103	0.095	0.085

† The doses absorbed were calculated by *RADDOSE-3D* (Zeldin *et al.*, 2013). ‡ The merging R factor $R_{\rm merge} = \sum_{hkl}\sum_i |I_i(hkl) - \langle I(hkl)\rangle| / \sum_{hkl}\sum_i I_i(hkl) \times 100$, where $I_i(hkl)$ is the intensity measured for a unique Bragg reflection with indices hkl and $\langle I(hkl)$ is the average intensity for multiple measurements of this reflection. § The multiplicity-independent R factor $R_{\rm meas} = \sum_{hkl}\{N(hkl)/[N(hkl)-1]\}^{1/2} \sum_i |I_i(hkl) - \langle I(hkl)\rangle| / \sum_{hkl}\sum_i I_i(hkl) \times 100$. ¶ The precision-independent R factor $R_{\rm p.i.m.} = \sum_{hkl}\{1/[N(hkl)-1]\}^{1/2} \sum_i |I_i(hkl) - \langle I(hkl)\rangle| / \sum_{hkl}\sum_i I_i(hkl) \times 100$, where $I_i(hkl)$ is the observed intensity, $\langle I(hkl)$ is the average intensity of multiple observations of symmetry-related reflections and $N(hkl)$ is the multiplicity (Weiss, 2001). †† According to Matthews (1968). ‡‡ $R_{\rm scaling}$ is the scaling R factor calculated with *SCALEIT* in *CCP*4 (Collaborative Computational Project, Number 4, 1994), between data set 1 and the other data sets.

0.414, respectively. $R_{\rm free}$ was calculated from a random 5% sample of the reflection data (Brünger, 1992). The model was further completed with *Coot* (Emsley *et al.*, 2010) using electron-density maps calculated with the phases obtained from the *SOLOMON* and *DM* calculations. The *Gi*SOR$_{\rm ih}$ model was refined using *PHENIX* v.1.8.4 (Adams *et al.*, 2010).

The structures of *Gi*SOR obtained from the various data sets collected on ID14-4 at ESRF were determined by molecular replacement with *Phaser* (McCoy *et al.*, 2005) as implemented in the *CCP*4 suite (Winn *et al.*, 2011; Collaborative Computational Project, Number 4, 1994) using the *Gi*SOR$_{\rm ih}$ structure as the search model. These structures were refined with *PHENIX* v.1.8.4 (Adams *et al.*, 2010). In the initial stages of refinement, individual coordinate and isotropic atomic displacement parameters (ADPs) were refined for all non-H protein atoms. After the initial refinement, manual building of the N-terminal region model with *Coot* against $\sigma_{\rm A}$-weighted $2|F_{\rm o}| - |F_{\rm c}|$ and $|F_{\rm o}| - |F_{\rm c}|$ electron-density maps was only possible from Lys16 onwards.

After the initial refinement cycles, solvent molecules were automatically added to the model and checked in *Coot* against $\sigma_{\rm A}$-weighted $2|F_{\rm o}| - |F_{\rm c}|$ and $|F_{\rm o}| - |F_{\rm c}|$ electron-density maps. In the final stages of refinement, translation–libration–screw (TLS; Winn *et al.*, 2001) rigid-body refinement of anisotropic atomic displacement parameters was used. Automated analysis of the refined isotropic ADPs by *PHENIX* led to the subdivision of the protein chain into the six TLS rigid bodies used in this refinement. The stereochemical quality of each model was assessed with *MolProbity* (Chen *et al.*, 2010). Although the refinement cycles were performed for all data sets (ds1–ds7), they were all revealed to be very similar to the structure from data set 1. For this reason, only the structure corresponding to data set 1 (here denoted *Gi*SOR), being the one obtained with the lowest X-ray exposure, is presented here and was deposited in the PDB.

2.5. Calculation of absorbed X-ray doses and difference Fourier electron-density maps

The X-ray doses absorbed by the crystal were calculated with *RADDOSE-3D* v.1.2.467 (Zeldin *et al.*, 2013) using the diffraction-weighted dose metric (DWD) and a cuboid-shaped crystal of 150 × 150 × 150 µm in size. For the *Gi*SOR crystal tested in-house the input parameters were as follows: Gaussian beam type with full width and half maximum of 240 and 240 µm; beam flux of 4.5×10^8 photons per second at 8.04 keV; 71100 s exposure time and 296.3° angular range. For the seven data sets for the *Gi*SOR crystal collected at the ESRF the input parameters were as follows: Gaussian beam type with full width and half maximum of 80 and 100 µm; beam flux of 1.7×10^{12} photons per second at 12.65 keV; the exposure times (s) for each data set are reported in Table 2, and the φ angles (wedge) are described above (§2.3).

To reveal the subtle structural differences between data set 1 (ds1) and the other data sets (ds2–ds7), their structure-factor amplitudes were scaled together using the *CCP*4 program *SCALEIT* (Collaborative Computational Project, Number 4, 1994; Howell & Smith, 1992) and placed on the same absolute scale. A difference Fourier electron-density map was then calculated using the *CCP*4 program *FFT* with coefficients $m[F_{{\rm obs}(n)} - F_{{\rm obs}(1)}]\exp[i\varphi_{{\rm calc}(1)}]$ (Winn *et al.*, 2011; Collaborative Computational Project, Number 4, 1994), where m is Read's figure of merit (Read, 1986), $F_{{\rm obs}(1)}$ and $F_{{\rm obs}(n)}$ are the observed structure-factor amplitudes from ds1 and the other data sets (n = 2–7), respectively, and $\varphi_{{\rm calc}(1)}$ is the calculated phase from the protein model refined against ds1.

2.6. Visible spectra analysis

The integration of the absorption peak at 646 nm in the absorption spectra shown in Fig. 1(*a*) was corrected taking into account the linear baseline between 800 and 1000 nm. Peak integration for all of the spectra was carried out between 450 and 800 nm and is presented as a function of the absorbed X-ray dose in Fig. 6.

2.7. Alignments

A profile alignment was performed using *ClustalX* (Thompson *et al.*, 1997), in which a sequence structural alignment of 1Fe-SORs (PDB entries 1do6, 2hvb and 3qzb) and *Gi*SOR was aligned against a structural sequence alignment of 2Fe-SORs (PDB entries 1dfx and 2ji1) and *Treponema pallidum* SOR (PDB entry 1y07). The two structural sequence alignments were obtained independently using *MODELLER* (Šali & Blundell, 1993).

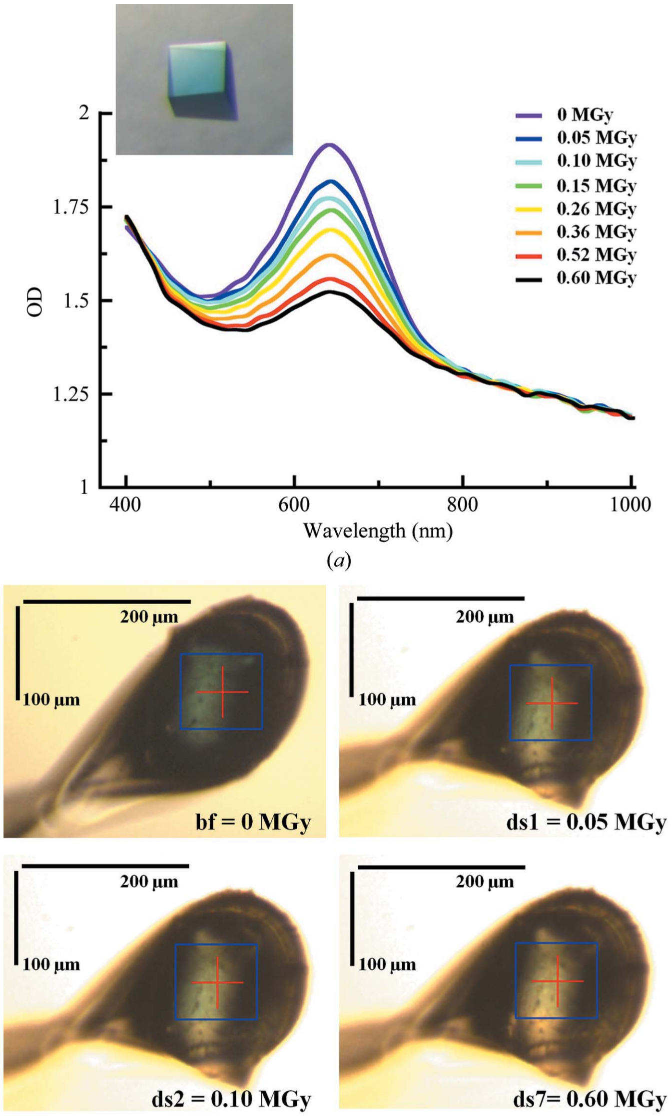

(*a*)

(*b*)

Figure 1
(*a*) Visible spectra of the *Gi*SOR crystal before (0 MGy) and after collecting each data set (the different doses are indicated). The intensity of the 647 nm absorption band characteristic of SOR in the oxidized state decreased on increased exposure to X-ray radiation. After the seventh data set, no further spectral changes were observed. Inset: *Gi*SOR crystal grown in the presence of 24%(*v*/*v*) dioxane. The largest crystal dimensions are ~0.15 × 0.15 × 0.15 mm. (*b*) Crystal snapshots showing the decay in the blue colour upon crystal exposure to the X-ray beam.

Table 3
Refinement statistics for *Gi*SOR.

Values in parentheses are for the highest resolution shell.

PDB code	4d7p
Resolution limits (Å)	31.90–2.00 (2.29–2.00)
R factor†	0.195 (0.233)
No. of reflections‡	8417 (2634)
Free *R* factor§	0.231 (0.318)
No. of reflections‡	405 (139)
Overall coordinate error estimate¶ (Å)	0.23
Model completeness and composition	
No. of molecules in asymmetric unit	1
Non-H protein atoms	792
Fe atoms	1
Solvent molecules	36
Mean *B* values†† (Å^2)	
Protein main chain	36.450
Protein side chain	41.586
Ions	37.830
Solvent molecules	37.071
Model r.m.s. deviation from ideality	
Bond lengths (Å)	0.012
Bond angles (°)	1.120
Chiral centres (Å^3)	0.044
Planar groups (Å)	0.006
Model validation‡‡	
Ramachandran outliers (%)	0.0
Ramachandran favoured (%)	97.87
Rotamer outliers (%)	0.0
C$^\beta$ outliers	0
Clashscore	0.67

† R factor = $\sum_{hkl} \big||F_{\rm obs}| - |F_{\rm calc}|\big| / \sum_{hkl} |F_{\rm obs}|$, where $|F_{\rm obs}|$ and $|F_{\rm calc}|$ are the observed and calculated structure-factor amplitudes, respectively. ‡ No $\sigma(F_{\rm o})$ cutoff. § Cross-validation R factor computed from a randomly chosen subset of 5% of the total number of reflections which were not used during refinement. ¶ Maximum-likelihood estimate. †† Calculated from isotropic or equivalent isotropic B values. ‡‡ As calculated with *MolProbity* (Chen *et al.*, 2010).

2.8. Accession numbers

The structure coordinates and structure factors for *Gi*SOR (data set 1) were deposited in the Protein Data Bank in Europe (Velankar *et al.*, 2012) with accession code 4d7p.

3. Results and discussion

The 1Fe-SOR from *G. intestinalis* (*Gi*SOR) is the first SOR from a eukaryotic organism to be investigated and is similar to other 1Fe-SORs (Testa *et al.*, 2011). The protein, with the iron centre in the oxidized state, crystallized in space group *I*23 with one molecule in the asymmetric unit. The structure obtained from the *Gi*SOR$_{\rm ih}$ data set was solved by the SAD method using the anomalous signal of the Fe atom in the collected X-ray data set and was refined to 1.95 Å resolution (Table 1). In spite of the high resolution and the overall good quality of the final electron-density maps, the electron density of residues 1–18 in the N-terminal region, including the glutamate and the lysine from the **EK**HxP motif, was poorly defined. This prevented the building of a structural model for this protein region.

Previous studies of prokaryotic SORs by X-ray crystallography and FTIR spectroscopy have shown that reduction of the iron active centre results in redox-linked structural changes involving the N-terminal region (Berthomieu *et al.*, 2002; Horch *et al.*, 2014; Yeh *et al.*, 2000). Moreover, the iron centre of *D. baarsii* 2Fe-SOR has been reported to be radiation-sensitive (Adam *et al.*, 2004). Based on this knowledge and the fact that the *Gi*SOR$_{\rm ih}$ data set was collected over 2 d, the poor electron density at the N-terminal region of the *Gi*SOR$_{\rm ih}$ structure was suggestive of structural disorder. This was probably owing to progressive X-ray-mediated photoreduction of the Fe atom during data collection, which takes place even when using X-rays from a rotating-anode source, with the crystal being exposed to a radiation dose of only 0.07 MGy.

In an attempt to obtain a three-dimensional structure of the protein with well defined electron density in the N-terminal region, the fact that *Gi*SOR crystallized in the high-symmetry cubic space group *I*23 was considered to be an advantage to enable the collection of a complete data set on the ID14-4 beamline at ESRF without radiation overexposure. Therefore, seven data sets of 40.25° (corresponding to 35 frames of 1.15° each) were collected from a single *Gi*SOR crystal with the same centred position and consecutive spindle rotation ranges. Before and after collecting each data set, the redox state of the catalytic Fe centre of the protein was assessed by acquiring visible absorption spectra of the crystal using an online microspectrophotometer coupled to the diffractometer (McGeehan *et al.*, 2009). The protein with iron in the oxidized, glutamate-bound state indeed exhibits a characteristic absorption band centred at 647 nm, the intensity of which decreases upon metal reduction (Fig. 1; Testa *et al.*, 2011).

As shown in Fig. 1(*a*), the intensity of this band (as well as the blue colour of the crystal; Fig. 1) decreased after the collection of each data set, suggesting progressive photoreduction of the metal upon exposure of the crystal to the X-ray beam. The decay occurred up to the seventh collected data set. A detailed analysis of crystal photoreduction is presented below (§3.4).

The iron reduction level in each data set was estimated by comparing the absorption spectra measured after each data acquisition with the spectrum acquired initially before exposure of the crystal to X-ray radiation (bf). The reduction level was found to increase from approximately 20% in the first data set, collected after exposing the crystal to X-rays for only 3.5 s (with a calculated absorbed dose of 0.05 MGy), to approximately 70% in the seventh data set (ds7; with a cumulative absorbed radiation dose of 0.60 MGy). Therefore,

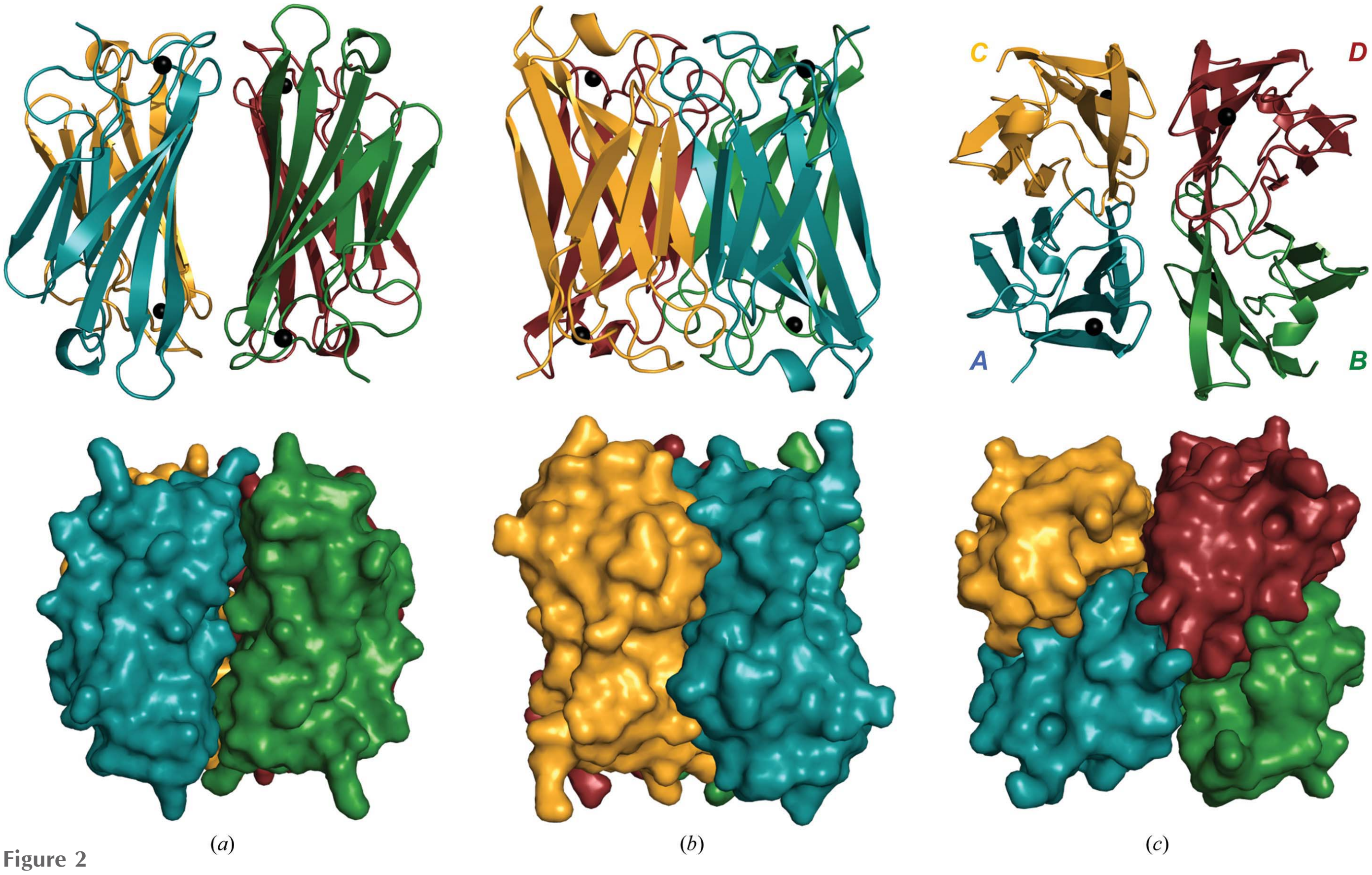

(*a*) (*b*) (*c*)

Figure 2
Cartoon (top) and surface (bottom) representations of the *Gi*SOR tetramer from different views. The representations in (*b*) and (*c*) are rotated by 90° about the horizontal and vertical axis in (*a*), respectively. Chains *A*, *B*, *C* and *D* are represented in blue, green, yellow and red, respectively. Fe atoms are represented as black spheres. The figures were generated with *PyMOL* (Schrödinger).

the structural model obtained from ds1 does not correspond to the fully oxidized state, but rather to a ‘partially reduced’ structure, and the structural model from ds7 nearly corresponds to a fully reduced state. However, for the sake of simplicity, we considered the structures obtained from ds1 and ds7 to be mainly representative of the oxidized and reduced states of the protein, respectively (see Table 2 for data-collection details and processing statistics). The structure of the ‘partially reduced’ oxidized enzyme (*Gi*SOR ds1) is discussed in detail below, and its overall refinement and final model-quality statistics are summarized in Table 3.

3.1. Overall assembly and monomer structure

When compared with the available SOR structures (Coelho *et al.*, 1997; Katona *et al.*, 2007; Yeh *et al.*, 2000; Adam *et al.*, 2004; Santos-Silva *et al.*, 2006), the structure of *Gi*SOR appears to be highly conserved (Fig. 2). A comparison using *Secondary Structure Matching* (*SSM*; Krissinel & Henrick, 2004), calculated between C$^{\alpha}$ atoms from aligned residues, with the other SOR monomers gives an r.m.s.d. of 1.5 Å, whereas a comparison with 1Fe-SOR tetramers results in an r.m.s.d. of 2.2 Å (Fig. 3). The electron-density map was of good quality overall, accounting for 86.5% (96 out of 111) of the protein amino-acid residues. Despite the short exposure time of the crystal to the X-ray beam, the electron density in the N-terminal region was still too poor to build a complete structural model of this region (from Met1 to Thr15), similar to *Gi*SOR$_{\rm ih}$, although electron density for His8 and Pro10 was now visible. This strongly suggests that the first 15 residues at the N-terminus of *Gi*SOR are highly flexible and thus structurally disordered in the crystallized protein. Nevertheless, at variance with *Gi*SOR$_{\rm ih}$, electron density for Glu17 and Lys18 of the **EK**HxP motif was now visible and could be modelled.

The asymmetric unit is constituted of a single monomer, with the inferred biological unit being a crystallographic

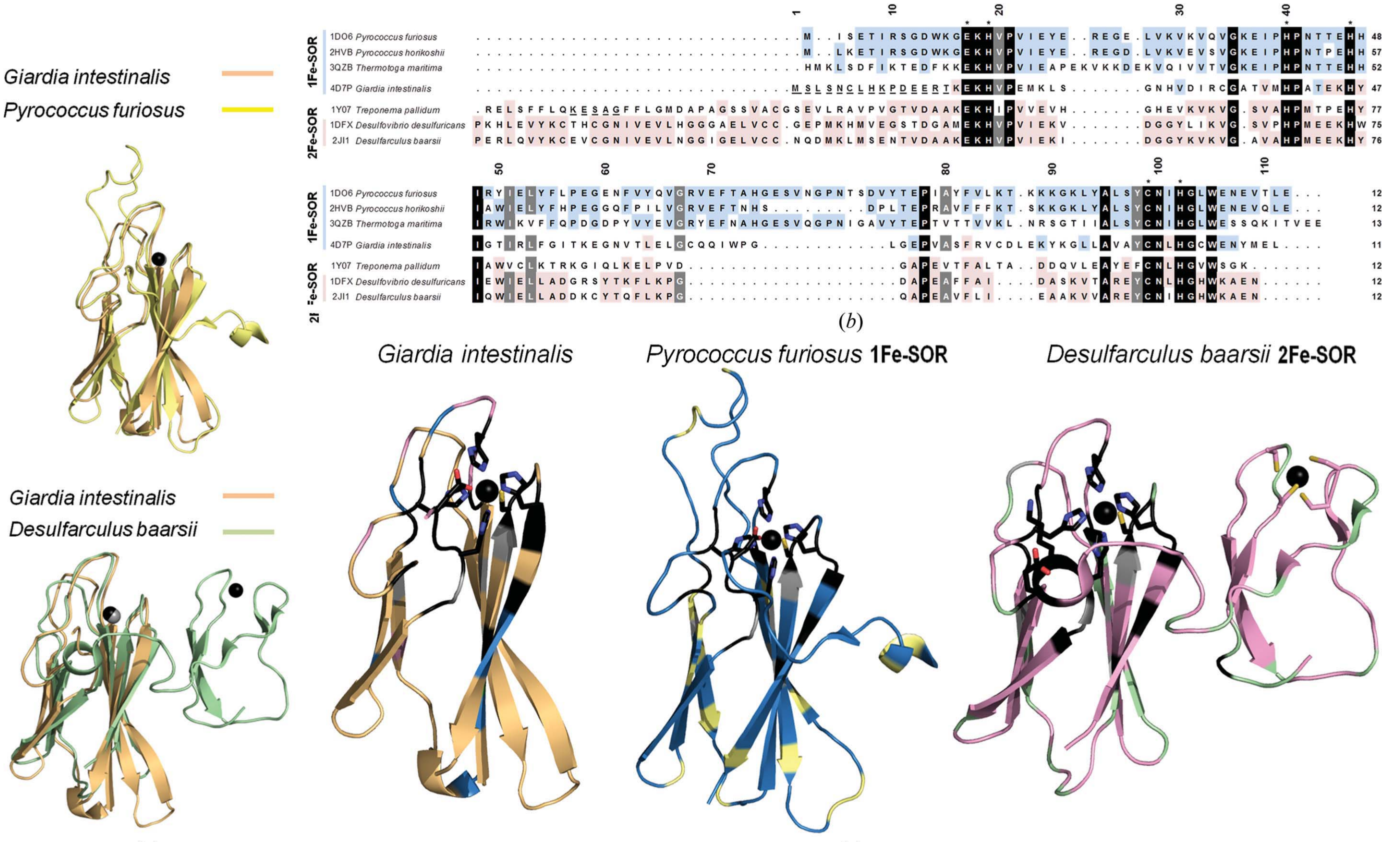

Figure 3
(*a*) Cartoon representation of *SSM* superposition of the *Gi*SOR monomer (orange) on subunit *B* of *P. furiosus* 1Fe-SOR (top; PDB entry 1do6; yellow; 1.4 Å r.m.s.d. calculated between C$^{\alpha}$ atoms of 94 aligned residues) and on subunit *A* of *D. baarsii* 2Fe-SOR (bottom; PDB entry 2ji1; green; 1.4 Å r.m.s.d. calculated between C$^{\alpha}$ atoms of 78 aligned residues). (*b*) *ClustalX* profile sequence alignment (Thompson *et al.*, 1997), using two independent sequence structural alignments: group 1 (top), 1Fe-SORs (PDB entries 1do6, 2hvb and 3qzb) and *Gi*SOR (PDB entry 4d7p); group 2 (bottom), 2Fe-SORs (PDB entries 1dfx and 2ji1) and *Treponema pallidum* SOR (PDB entry 1y07). The strictly conserved amino acids are represented as black boxes, whereas the dark grey boxes represent residues that are mostly conserved among the selected sequences. Blue boxes represent residues that are conserved among the 1Fe-SORs and pink boxes represent those that are conserved among the 2Fe-SORs and *T. pallidum* SOR. (*c*) *Gi*SOR, *P. furiosus* 1Fe-SOR and *D. baarsii* 2Fe-SOR monomers are represented in the same base colours as in (*a*), but with the amino acids conserved in the 1Fe-SOR group shown in blue and those conserved among the 2Fe-SOR group shown in pink; the black and dark grey regions are as in (*b*). The cartoon representations of the monomers were generated with *PyMOL* (Schrödinger). The sequence identities of *Gi*SOR to the other SORs are 1do6, 41%; 2hvb, 43%; 3qzb, 36%; 1y07, 31%; 1dfx, 20%; 2ji1, 30%. The underlined amino-acid residues in *Gi*SOR and *T. pallidum* SOR (PDB entry 1y07) were not modelled in the respective crystal structures.

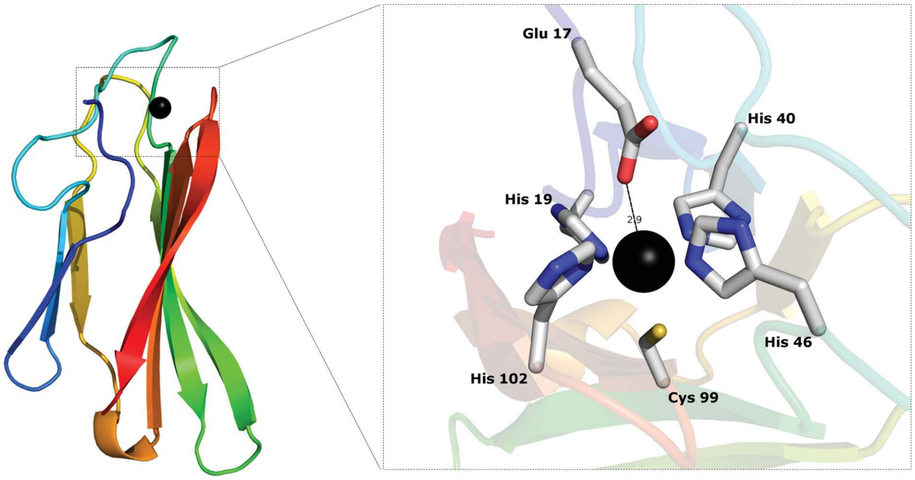

Figure 4
Cartoon representation of the *Gi*SOR monomer rainbow-coloured from the N-terminus (blue) to the C-terminus (red). The inset shows a detailed view of the *Gi*SOR active site. The Fe atom (represented as a black sphere) is octahedrally coordinated by six residues. The iron–ligand distances are 2.04 Å to His19 $N^{\varepsilon2}$, 2.23 Å to His40 $N^{\varepsilon2}$, 2.11 Å to His46 $N^{\varepsilon2}$, 2.34 Å to His102 $N^{\delta1}$, 2.37 Å to Cys99 S^{γ} and 2.86 Å to Glu17 $O^{\varepsilon2}$. The figures were generated with *PyMOL* (Schrödinger).

tetramer, in agreement with previous biochemical studies (Testa *et al.*, 2011; Fig. 2). The tetramer has an approximately cubic shape with a ~50 Å edge and its geometrical centre is located at one of the special positions in space group *I*23 with 222 point-group symmetry. Within each tetramer, the subunits mainly interact through electrostatic interactions and hydrogen bonds. The *Gi*SOR tetramer includes a total of 328 hydrogen bonds as calculated with *HBPLUS* (McDonald & Thornton, 1994); of these, only 40 are located in the interface between different subunits (Supplementary Table S1). There are more interacting residues between homodimers *AC* and *BD* than between homodimers *AB* and *CD*, accounting for 32 and four residues, respectively. Conversely, subunits *AD* and *BC* share only four hydrogen bonds (Fig. 2, Supplementary Table S1).

Similarly to other SORs (both 1Fe-SORs and the catalytic domains of 2Fe-SORs), the *Gi*SOR monomer adopts an immunoglobulin-like fold organized into a seven-stranded β-barrel (Figs. 3 and 4; Yeh *et al.*, 2000; Katona *et al.*, 2007; Coelho *et al.*, 1997) with the following topology: β_1 (Pro21–Ser26), β_2 (His29–Cys34), β_5 (Val79–Arg83) and β_3 (Ile48–Thr57), β_4 (Thr63–Gln70), β_6 (Tyr90–Cys99), β_7 (Gly103–Glu110).

The only structural differences in the monomer between *Gi*SOR and the SORs presented in Fig. 3 are the shorter loop connecting the strands β_4 and β_5 and the presence of a 3_{10}-helix (Leu87–Lys89) located between the β_5 and β_6 strands in *Gi*SOR. The presence of a 3_{10}-helix has also been reported in other SOR structures such as *P. furiosus* 1Fe-SOR (Yeh *et al.*, 2000), but at the N-terminal loop. In the case of *Gi*SOR, owing to the low quality of the electron density in the N-terminal region, we cannot rule out that a 3_{10}-helix is also present in this region.

Hydrophobicity analysis of *Gi*SOR indicates that hydrophobic residues are mainly located in the internal part of the monomer, as for the other SORs presented in Fig. 3(*b*). However, the grand average of hydropathicity (GRAVY; Kyte & Doolittle, 1982) is −0.3, which is more similar to the values typical of 2Fe-SORs (~−0.3) than to those reported for 1Fe-SORs (~−0.5) and *T. pallidum* SOR (0.07).

Despite the higher structural homology, there is a lower sequence homology between *Gi*SOR and the other 1Fe-SORs (Figs. 3*b* and 3*c*). The highly conserved residues include the amino-acid residues involved in iron coordination at the catalytic centre and a few other residues in the proximity of the iron centre. Besides these, *Gi*SOR does not share a high degree of sequence homology with other SORs, as illustrated in Figs. 3(*b*) and 3(*c*). Interestingly, *Gi*SOR contains more cysteine residues than any of the other SORs. Besides the cysteine that is coordinating the catalytic iron, the 1Fe-SORs presented in Fig. 3(*b*) do not contain any other cysteines. The other SORs, including the 2Fe-SORs and *T. pallidum* SOR, contain only one additional cysteine (Cys88 in *D. baarsii* and Cys82 in *T. pallidum*). In contrast, *Gi*SOR contains a total of five Cys residues (numbered 6, 34, 68, 85 and 104; Fig. 3*b*). Cys68 is located at the centre of the tetramer, facing the other symmetry-related cysteines with a closest distance of 6.4 Å between Cys68 S^{γ} in subunit *A* and its equivalent residue in subunit *B*. The presence of all of these cysteines could be related to the fact that the protein is from a eukaryote, and thus these residues could be involved in cell redox signalling.

3.2. The iron centre

Each *Gi*SOR monomer displays a solvent-exposed active site containing one Fe atom. The high solvent accessibility of the metal has been proposed to be important for the catalytic function of the enzyme, as it ensures easy access of superoxide anion to the active site and its prompt reduction to hydrogen peroxide (Pinto *et al.*, 2010; Sheng *et al.*, 2014). The Fe atom displays octahedral coordination geometry (Fig. 4) and is coordinated by residues located in loops connecting β-strands: the imidazole rings of His19, His40, His46 and His102 in the equatorial plane, with the Cys99 S atom and one carboxylate O atom from Glu17 occupying the two axial positions. Similarly to other SORs, all histidine ligands coordinate the iron through their $N^{\varepsilon2}$ atom, except for His102, which binds the metal through the $N^{\delta1}$ atom. This is the 'closed conformation' typical of SOR in the ferric form, as previously observed for the *Pyrococcus* enzymes (Yeh *et al.*, 2000).

3.3. Radiation damage

One of the limiting aspects of macromolecular X-ray crystallography is the radiation damage related to the ionizing nature of the incident X-ray beam. This problem can be partially overcome by collecting diffraction data at 100 K, thus minimizing the diffusion of the free-radical species responsible for secondary damage (Weik & Colletier, 2010). However, with the beam intensity available at third-generation synchrotrons, radiation damage still occurs even at cryogenic temperatures (Burmeister, 2000; Weik & Colletier, 2010; Garman & Owen, 2006). The global indicators of radiation damage are a decreased diffraction resolution limit, increased mosaicity and Wilson *B* factors and unit-cell expansion observed at increasing X-ray doses (Ravelli & McSweeney, 2000).

The *Gi*SOR crystal was exposed to the X-ray beam during the collection of seven independent data sets, the processing statistics of which are reported in Table 2. Analysis of these values indicates that the data quality decreases from ds1 to ds3, while on the contrary it counterintuitively increases from ds4 to ds7, as shown by the $R_{\rm merge}$ and data-resolution values. However, during the different data collections the crystal was continuously rotated to homogenously increase the dose absorbed by the core of the sample. Therefore, the variations of global radiation damage indicators have poor significance in this range of absorbed doses (from 0.05 to 0.60 MGy) and rather reflect the anisotropy of crystalline quality with the rotation of the spindle. Moreover, these indicators typically fail to describe the early stages of radiation damage related to specific structural damage (Ravelli & McSweeney, 2000).

In order to assess the probable structural changes induced at such low doses, since the structure refinement itself did not provide evidence for structural differences at the iron, difference Fourier electron-density maps between the first data set and each of the subsequent data sets (ds$_n$, $n = 2$–7) were calculated using the phases of the refined *Gi*SOR structure (ds1). This method is known to reveal very subtle radiation-induced structural modifications (Burmeister, 2000; Ravelli & McSweeney, 2000; Weik *et al.*, 2000). The first difference Fourier map did not reveal any detectable change in the electron density at the iron centre for very low absorbed doses (0.10 MGy as calculated with *RADDOSE-3D*; Zeldin *et al.*, 2013; Fig. 5), thereby suggesting that the structures obtained at the lowest doses (ds1 and ds2) are presumably close to the native state. The next difference Fourier map calculated with data sets 3–7 clearly revealed progressive X-ray-induced reduction at the active site, with negative electron-density peaks at Glu17 O$^{\varepsilon 2}$ and Cys99 S$^{\gamma}$ growing as the absorbed dose increased (from 0.15 to 0.60 MGy; Fig. 5). The lack of electron density at the carboxyl group of Glu17 was interpreted as resulting from a chemical modification rather than a repositioning of the glutamate, since no counterpart positive density appeared close by in the map. In addition, the clear location of this peak on one of the carboxylate O atoms suggests an X-ray-induced transformation into an aldehyde or a primary alcohol moiety, rather than a classical decarboxylation. The typical damage rapidly affecting the S atom of Cys99 suggests that the active-site region is particularly sensitive to X-rays compared with the rest of the structure. The negative peak which appears near the catalytic iron centre could be attributed to a slight displacement of the iron; however, this density is not counterbalanced by any positive peak. A positive peak near His46 N$^{\varepsilon 2}$ weakly appearing in ds4 (after a dose of 0.26 MGy) and becoming more evident in ds7 is not matched by any negative peak close by (Fig. 5). This observation is difficult to interpret; however, the ds7 map appears to be noisier than the other maps, probably owing to the extent of modifications in the active site at this high radiation

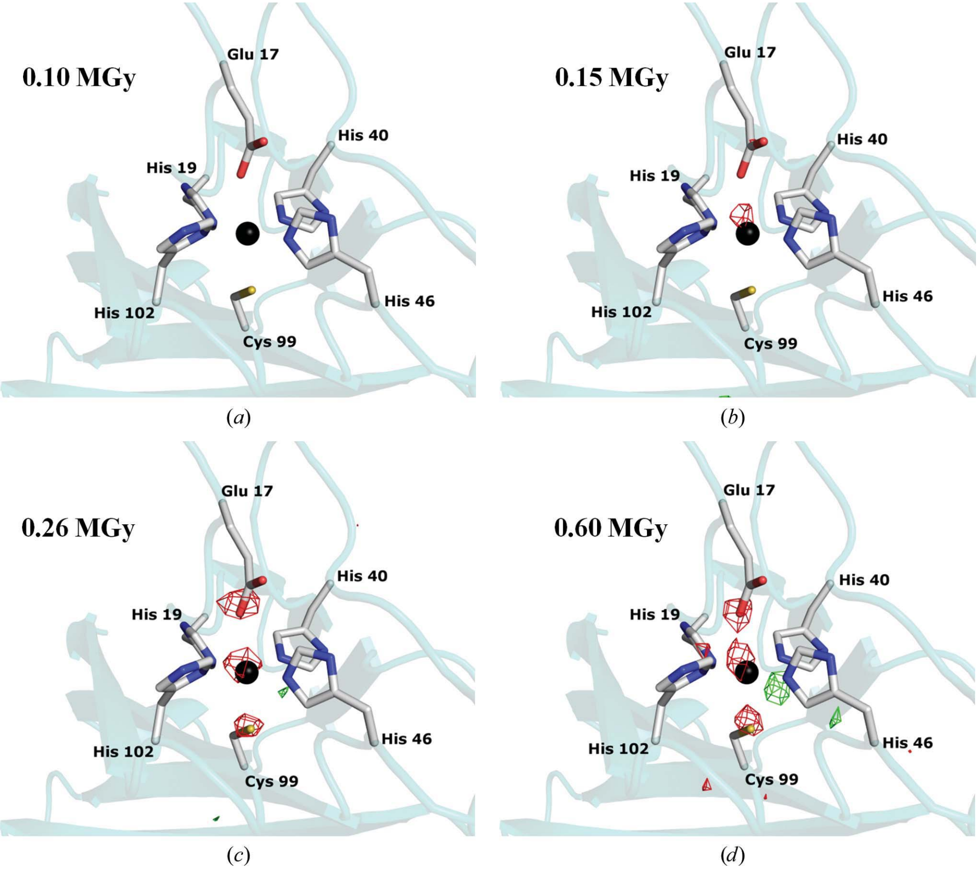

(*a*) (*b*)

(*c*) (*d*)

Figure 5
Difference Fourier electron-density maps of the *Gi*SOR active site between (*a*) data sets 2 and 1, (*b*) data sets 3 and 1, (*c*) data sets 4 and 1 and (*d*) data sets 7 and 1. The Fe atom is represented as a black sphere. The negative (red) and positive (green) peaks are contoured at -4.0σ and 4.0σ, respectively. The figures were generated with *PyMOL* (Schrödinger).

dose, which makes the analysis difficult. Besides these residues located in the active-centre region, other residues exhibited signs of radiation damage, as revealed by the negative peaks at the terminal groups of Glu44 (contoured at -5.1σ) and Cys68 (contoured at -7.6σ) observed in data set 7. This is in agreement with the fact that the residues most susceptible to radiation damage are typically acidic and sulfur-containing groups, as well as the catalytic residues, which are often in 'weak links' or 'strained' configurations to perform their catalytic function (Weik *et al.*, 2000). In a similar crystallographic study on acetylcholinesterase from *Torpedo californica* (TcAChE; Ravelli & McSweeney, 2000), electron-density loss for the catalytic Glu306 was detected before observing decay in the crystal diffraction resolution limit, while a histidine residue (His406) in the proximity of this glutamate did not show any electron-density decrease (Ravelli & McSweeney, 2000). The same scenario apparently applies to the active site of *Gi*SOR, for which radiation damage appears at a relatively low absorbed dose in ds3 (0.15 MGy) and evolves during collection of data sets 4–7 at an absorbed dose increasing from 0.26 to 0.60 MGy. It should be noted that such an absorbed dose is two orders of magnitude below the experimental dose limit (30 MGy) at which damage is considered to compromise the veracity of the structure (Owen *et al.*, 2006; Henderson, 1990). In conclusion, our data suggest that crystalline *Gi*SOR is extremely sensitive to X-ray radiation, as previously reported for similar proteins (Adam *et al.*, 2004; Yeh *et al.*, 2000).

3.4. Photoreduction

In previous studies (Berthomieu *et al.*, 2002; Horch *et al.*, 2014; Yeh *et al.*, 2000), SOR was suggested to undergo redox-linked conformational changes upon iron reduction. When the iron is in the reduced (ferrous) state, the active site was shown to be in an 'open conformation' with the axial coordination position vacant and available for superoxide anion binding. After reacting with superoxide anion, and following the release of hydrogen peroxide, a glutamate was found to bind to the oxidized iron as a result of a loop movement, locking the active site in a 'closed conformation'.

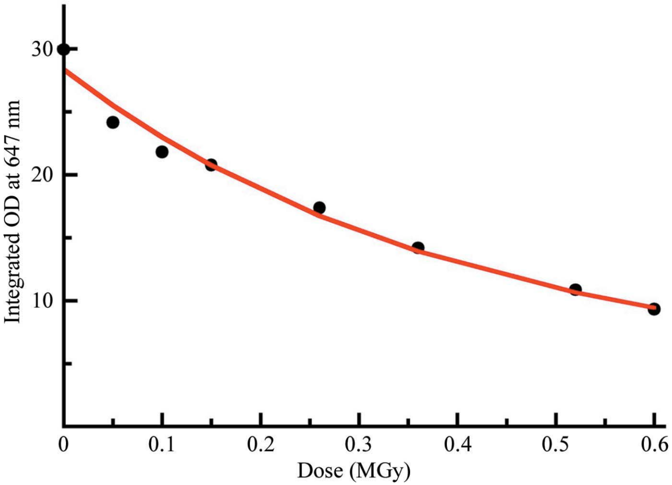

Figure 6
X-ray-induced reduction of crystallized *Gi*SOR. The radiation-dose dependence of the integrated absorption peak at 647 nm is plotted against optical density (OD) values, with their best fit to a mono-exponential decay represented in red.

As already mentioned, and based on the absorption spectra displayed in Fig. 1(*a*), in *Gi*SOR 20% to approximately 70% of the catalytic iron was found to be photoreduced on X-ray exposure (from ds1 to ds7). Consistently, the irradiated crystal progressively lost its characteristic bluish colour and eventually became almost colourless at the position where it had been centred for data collection (Fig. 1*b*).

The decay of the 647 nm absorption band as a function of the absorbed X-ray dose is shown in Fig. 6. The curve is fitted by an exponential regression, $\mathrm{OD}(D) = \mathrm{OD}_0\exp(-D/D_0)$, where D is the dose, OD_0 is the initial amplitude at zero dose and D_0 is the decay constant. The data are suitably modelled with a single exponential decay with $D_0^{-1} \simeq 0.4$ MGy. The decrease in absorption between 0 and 0.05 MGy suggests a secondary contribution by a non-deconvolutable fast process. In conclusion, the X-ray-induced reduction of *Gi*SOR appears to be two orders of magnitude faster overall than the experimental dose limit (30 MGy) and thus definitely distinct from the standard radiation-damage pattern (Carpentier *et al.*, 2010; Ravelli & McSweeney, 2000; Weik *et al.*, 2000). A rapid reduction rate of iron centres (below 1 MGy) has previously been described for several haem proteins (Beitlich *et al.*, 2007), consistent with that computed here for *Gi*SOR. Double exponential decay has been successfully extracted from the data of Beitlich and coworkers, and the idea that iron-centre reduction could be related to mobile solvated electrons is probably also applicable to *Gi*SOR. The rapid reduction phase is owing to the increased accumulation of solvated electrons when the sample is illuminated, whereas the distinct slower rate is related to a steady state in which removal of solvated electrons balances their production. Finally, our observations clearly corroborate the conclusions of Beitlich and coworkers emphasizing that protein redox centres are potentially high attractors for X-ray-generated solvated photoelectrons and thus are rapidly subject to radiation damage. Therefore, X-ray crystallographic studies on such proteins should be complemented with spectroscopic measurements, as implemented in this and previous work (Adam *et al.*, 2004).

The structures determined at increasing iron-reduction levels invariably revealed poor electron density in the N-terminal region of the protein, as if this region was highly flexible and thus able to adopt different conformations in the crystal lattice regardless of the metal redox state. In spite of this flexibility, at variance with other SORs, no differences were observed in the position of the iron-coordinating residues in *Gi*SOR, including Glu17, which indeed retained its position in all structures. Nevertheless, the iron–glutamate distance increased from 2.86 Å in the ds1 structure to 3.02 Å in the ds7 structure.

In conclusion, exposure of the *Gi*SOR crystal to the ESRF ID14-4 X-ray beam for ∼40 s (0.60 MGy) resulted in near-complete disappearance of the 647 nm absorption band (Figs. 1 and 6), clearly indicating photoreduction of the crystallized protein. A similar effect was observed in 2Fe-SOR from *D. baarsii* (Adam *et al.*, 2004), where it was proposed to induce an average backwards motion of the equatorial ligands, causing an active-site expansion (Adam *et al.*, 2004). In contrast, the difference Fourier electron-density maps calculated for *Gi*SOR did not suggest any structural change at the level of the iron-coordinating ligands.

The work presented here shows that X-ray-induced iron photoreduction in *Gi*SOR does not induce the conversion of the 'closed' conformation into the 'open' conformation, which is at variance with that observed for other SORs by other methods (Berthomieu *et al.*, 2002; Horch *et al.*, 2014). One possible explanation could be that this type of structural rearrangement may not occur at 100 K.

Temperature-controlled kinetic crystallography using X-ray radiation to trigger catalytic reactions has been used in structural biology to characterize reaction intermediates (Bourgeois & Royant, 2005). However, the cryogenic temperatures (∼180–200 K) used to avoid free-radical diffusion during data collection clearly limit protein dynamics (Weik & Colletier, 2010), thus preventing the formation of catalytic intermediates in the crystallized protein after reaction is initiated. Nevertheless, the structures of catalytic intermediates have been successfully obtained at higher temperatures, at which protein dynamics are enhanced (Weik & Colletier, 2010; Baxter *et al.*, 2004; Bourgeois & Royant, 2005; Schlichting *et al.*, 2000; Colletier *et al.*, 2008). To the best of our knowledge, experiments of this kind have not yet been attempted on SORs. In future work, it will be interesting to use *Gi*SOR as a model to structurally characterize catalytic intermediates by kinetic X-ray crystallography, with the aim of acquiring new knowledge on the reaction mechanism of SOR.

4. Conclusions

Superoxide reductase is a metalloenzyme that is widespread in prokaryotic organisms and is responsible for the detoxification of superoxide anion to hydrogen peroxide. Here, we have reported the first three-dimensional structure of an SOR from a eukaryotic organism, the protozoan parasite *G. intestinalis*. The photoreduction of the protein metal centre by the high-intensity synchrotron X-ray radiation was monitored by means of an online microspectrophotometer coupled to the diffractometer. The 2.0 Å resolution structure shows that *Gi*SOR is structurally similar to other 1Fe-SORs characterized to date. The protein forms a tetrameric assembly with 222 point-group symmetry, in which the monomers display the characteristic immunoglobulin β-barrel fold. At variance with the prokaryotic SORs structurally characterized to date, the *G. intestinalis* enzyme displays an unusually high flexibility of the N-terminal region and a 3_{10}-helix located in a region connecting two β-strands in the barrel. Similarly to other 1Fe-SORs, in the oxidized protein the Fe atom is coordinated by six ligand residues with an octahedral geometry. However, surprisingly, no redox-linked structural changes were observed upon photoreduction of the iron centre. Moreover, the enzyme revealed a remarkably high susceptibility to radiation damage. In particular, after absorbing a radiation dose of only 0.15 MGy, far below the experimental dose limit of 30 MGy (Owen *et al.*, 2006), the residues involved in the catalytic centre, namely Glu17, were found to be affected upon exposure to the increased X-ray dose. Nevertheless, they retained their position regardless of the metal-oxidation state. It cannot be ruled out that the lack of structural rearrangements in response to metal reduction may arise from constraints in the crystal lattice, that the appearance of radiation damage may impair the redox-driven structural conformation changes, or even that this structural rearrangement may not occur at 100 K.

Therefore, it remains to be clarified whether redox-linked structural change in SORs can be followed by an online microspectrophotometer using X-ray crystallography.

Acknowledgements

This work was supported by Fundação para a Ciência e Tecnologia of Portugal (PTDC/BIA-PRO/111940/2009 and PEst-OE/EQB/LA0004/2013) and by Ministero dell'Istruzione, dell'Università e della Ricerca of Italy (PNR-CNR Aging Program 2012–2014 to AG, FIRB RBIN06E9Z8 and PRIN 20107Z8XBW_005 to PS). FGP was supported by an iBET fellowship; CMS was supported by a BI fellowship within FCT grant PTDC/BIA-PRO/111940/2009. CVR is a recipient of SFRH/BPD/94050/2013. We thank the ESRF and the ID14-4 beamline staff, Grenoble, France for support during the synchrotron data collections. We also acknowledge a bilateral grant award from Consiglio Nazionale delle Ricerche of Italy and Fundação para a Ciência e Tecnologia of Portugal. We thank the anonymous referees for their many constructive comments and suggestions, which were very helpful in improving this manuscript.

References

Abrahams, J. P. & Leslie, A. G. W. (1996). *Acta Cryst.* D**52**, 30–42.

Abreu, I. A., Saraiva, L. M., Soares, C. M., Teixeira, M. & Cabelli, D. E. (2001). *J. Biol. Chem.* **276**, 38995–39001.

Adam, V., Royant, A., Nivière, V., Molina-Heredia, F. P. & Bourgeois, D. (2004). *Structure*, **12**, 1729–1740.

Adams, P. D. *et al.* (2010). *Acta Cryst.* D**66**, 213–221.

Baxter, R. H., Seagle, B. L., Ponomarenko, N. & Norris, J. R. (2004). *J. Am. Chem. Soc.* **126**, 16728–16729.

Beitlich, T., Kühnel, K., Schulze-Briese, C., Shoeman, R. L. & Schlichting, I. (2007). *J. Synchrotron Rad.* **14**, 11–23.

Berthomieu, C., Dupeyrat, F., Fontecave, M., Verméglio, A. & Nivière, V. (2002). *Biochemistry*, **41**, 10360–10368.

Bertini, I. (1994). *Bioinorganic Chemistry.* Mill Valley: University Science Books.

Bourgeois, D. & Royant, A. (2005). *Curr. Opin. Struct. Biol.* **15**, 538–547.

Brünger, A. T. (1992). *Nature (London)*, **355**, 472–475.

Burmeister, W. P. (2000). *Acta Cryst.* D**56**, 328–341.

Carpentier, P., Royant, A., Weik, M. & Bourgeois, D. (2010). *Structure*, **18**, 1410–1419.

Chen, V. B., Arendall, W. B., Headd, J. J., Keedy, D. A., Immormino, R. M., Kapral, G. J., Murray, L. W., Richardson, J. S. & Richardson, D. C. (2010). *Acta Cryst.* D**66**, 12–21.

Chen, L., Sharma, P., Le Gall, J., Mariano, A. M., Teixeira, M. & Xavier, A. V. (1994). *Eur. J. Biochem.* **226**, 613–618.

Clay, M. D., Jenney, F. E. Jr, Hagedoorn, P. L., George, G. N., Adams, M. W. W. & Johnson, M. K. (2002). *J. Am. Chem. Soc.* **124**, 788–805.

Coelho, A. V., Matias, P., Fülöp, V., Thompson, A., Gonzalez, A. & Carrondo, M. A. (1997). *J. Biol. Inorg. Chem.* **2**, 680–689.

Collaborative Computational Project, Number 4 (1994). *Acta Cryst.* D**50**, 760–763.

Colletier, J.-P., Bourgeois, D., Sanson, B., Fournier, D., Sussman, J. L., Silman, I. & Weik, M. (2008). *Proc. Natl Acad. Sci. USA*, **105**, 11742–11747.

Cowtan, K. (1994). *Jnt CCP4/ESF–EACBM Newsl. Protein Crystallogr.* **31**, 34–38.

Emsley, P., Lohkamp, B., Scott, W. G. & Cowtan, K. (2010). *Acta Cryst.* D**66**, 486–501.

Ericsson, U. B., Hallberg, B. M., DeTitta, G. T., Dekker, N. & Nordlund, P. (2006). *Anal. Biochem.* **357**, 289–298.

Fridovich, I. (1997). *J. Biol. Chem.* **272**, 18515–18517.

Garman, E. F. & Owen, R. L. (2006). *Acta Cryst.* D**62**, 32–47.

Halliwell, B. (2007). *Biochem. Soc. Trans.* **35**, 1147–1150.

Halliwell, B. & Gutteridge, J. M. (1984). *Biochem. J.* **219**, 1–14.

Henderson, R. (1990). *Proc. R. Soc. B Biol. Sci.* **241**, 6–8.

Horch, M., Pinto, A. F., Utesch, T., Mroginski, M. A., Romão, C. V., Teixeira, M., Hildebrandt, P. & Zebger, I. (2014). *Phys. Chem. Chem. Phys.* **16**, 14220–14230.

Howell, P. L. & Smith, G. D. (1992). *J. Appl. Cryst.* **25**, 81–86.

Imlay, J. A. (2003). *Annu. Rev. Microbiol.* **57**, 395–418.

Jenney, F. E. Jr, Verhagen, M. F., Cui, X. & Adams, M. W. W. (1999). *Science*, **286**, 306–309.

Kabsch, W. (2010). *Acta Cryst.* D**66**, 125–132.

Katona, G., Carpentier, P., Nivière, V., Amara, P., Adam, V., Ohana, J., Tsanov, N. & Bourgeois, D. (2007). *Science*, **316**, 449–453.

Krissinel, E. & Henrick, K. (2004). *Acta Cryst.* D**60**, 2256–2268.

Kyte, J. & Doolittle, R. F. (1982). *J. Mol. Biol.* **157**, 105–132.

Lombard, M., Fontecave, M., Touati, D. & Nivière, V. (2000). *J. Biol. Chem.* **275**, 115–121.

Lombard, M., Touati, D., Fontecave, M. & Nivière, V. (2000). *J. Biol. Chem.* **275**, 27021–27026.

Lucchetti-Miganeh, C., Goudenège, D., Thybert, D., Salbert, G. & Barloy-Hubler, F. (2011). *BMC Microbiol.* **11**, 105.

Matthews, B. W. (1968). *J. Mol. Biol.* **33**, 491–497.

McCarthy, A. A., Brockhauser, S., Nurizzo, D., Theveneau, P., Mairs, T., Spruce, D., Guijarro, M., Lesourd, M., Ravelli, R. B. G. & McSweeney, S. (2009). *J. Synchrotron Rad.* **16**, 803–812.

McCoy, A. J., Grosse-Kunstleve, R. W., Storoni, L. C. & Read, R. J. (2005). *Acta Cryst.* D**61**, 458–464.

McDonald, I. K. & Thornton, J. M. (1994). *J. Mol. Biol.* **238**, 777–793.

McGeehan, J., Ravelli, R. B. G., Murray, J. W., Owen, R. L., Cipriani, F., McSweeney, S., Weik, M. & Garman, E. F. (2009). *J. Synchrotron Rad.* **16**, 163–172.

Moura, I., Tavares, P., Moura, J. J. G., Ravi, N., Huynh, B. H., Liu, M.-Y. & LeGall, J. (1990). *J. Biol. Chem.* **265**, 21596–21602.

Niesen, F. H., Berglund, H. & Vedadi, M. (2007). *Nature Protoc.* **2**, 2212–2221.

Nivière, V. & Fontecave, M. (2004). *J. Biol. Inorg. Chem.* **9**, 119–123.

Owen, R. L., Rudiño-Piñera, E. & Garman, E. F. (2006). *Proc. Natl Acad. Sci. USA*, **103**, 4912–4917.

Pape, T. & Schneider, T. R. (2004). *J. Appl. Cryst.* **37**, 843–844.

Perrakis, A., Morris, R. & Lamzin, V. S. (1999). *Nat. Struct. Biol.* **6**, 458–463.

Pinto, A. F., Rodrigues, J. V. & Teixeira, M. (2010). *Biochim. Biophys. Acta*, **1804**, 285–297.

Ravelli, R. B. G. & McSweeney, S. M. (2000). *Structure*, **8**, 315–328.

Read, R. J. (1986). *Acta Cryst.* A**42**, 140–149.

Šali, A. & Blundell, T. L. (1993). *J. Mol. Biol.* **234**, 779–815.

Santos, S. P., Bandeiras, T. M., Pinto, A. F., Teixeira, M., Carrondo, M. A. & Romão, C. V. (2012). *Protein Expr. Purif.* **81**, 193–200.

Santos-Silva, T., Trincão, J., Carvalho, A. L., Bonifácio, C., Auchère, F., Raleiras, P., Moura, I., Moura, J. J. G. & Romão, M. J. (2006). *J. Biol. Inorg. Chem.* **11**, 548–558.

Schieber, M. & Chandel, N. S. (2014). *Curr. Biol.* **24**, R453–R462.

Schlichting, I., Berendzen, J., Chu, K., Stock, A. M., Maves, S. A., Benson, D. E., Sweet, R. M., Ringe, D., Petsko, G. A. & Sligar, S. G. (2000). *Science*, **287**, 1615–1622.

Schneider, T. R. & Sheldrick, G. M. (2002). *Acta Cryst.* D**58**, 1772–1779.

Sheldrick, G. M. (2002). *Z. Kristallogr.* **217**, 644–650.

Sheldrick, G. M. (2008). *Acta Cryst.* A**64**, 112–122.

Sheng, Y., Abreu, I. A., Cabelli, D. E., Maroney, M. J., Miller, A. F., Teixeira, M. & Valentine, J. S. (2014). *Chem. Rev.* **114**, 3854–3918.

Testa, F., Mastronicola, D., Cabelli, D. E., Bordi, E., Pucillo, L. P., Sarti, P., Saraiva, L. M., Giuffrè, A. & Teixeira, M. (2011). *Free Radical Biol. Med.* **51**, 1567–1574.

Thompson, J. D., Gibson, T. J., Plewniak, F., Jeanmougin, F. & Higgins, D. G. (1997). *Nucleic Acids Res.* **25**, 4876–4882.

Velankar, S. *et al.* (2012). *Nucleic Acids Res.* **40**, D445–D452.

Vonrhein, C., Blanc, E., Roversi, P. & Bricogne, G. (2007). *Methods Mol. Biol.* **364**, 215–230.

Weik, M. & Colletier, J.-P. (2010). *Acta Cryst.* D**66**, 437–446.

Weik, M., Ravelli, R. B. G., Kryger, G., McSweeney, S., Raves, M. L., Harel, M., Gros, P., Silman, I., Kroon, J. & Sussman, J. L. (2000). *Proc. Natl Acad. Sci. USA*, **97**, 623–628.

Weiss, M. S. (2001). *J. Appl. Cryst.* **34**, 130–135.

Winn, M. D. *et al.* (2011). *Acta Cryst.* D**67**, 235–242.

Winn, M. D., Isupov, M. N. & Murshudov, G. N. (2001). *Acta Cryst.* D**57**, 122–133.

Yeh, A. P., Hu, Y., Jenney, F. E. Jr, Adams, M. W. W. & Rees, D. C. (2000). *Biochemistry*, **39**, 2499–2508.

Zeldin, O. B., Gerstel, M. & Garman, E. F. (2013). *J. Appl. Cryst.* **46**, 1225–1230.